Applied Clay Science 184 (2020) 105407

Contents lists available at ScienceDirect

Applied Clay Science

journal homepage: www.elsevier.com/locate/clay

Research paper

# Adsorption of iodate on nanosized tubular halloysite

Wenbin Yu[a,b], Huifang Xu[b,*], Daoyong Tan[c], Yihang Fang[b], Eric E. Roden[b], Quan Wan[a,d]

[a] State Key Laboratory of Ore Deposit Geochemistry, Institute of Geochemistry, Chinese Academy of Sciences, Guiyang, Guizhou 550081, China
[b] Department of Geoscience, University of Wisconsin–Madison, Madison, WI 53706, United States
[c] Key Laboratory of Solid Waste Treatment and Resource Recycle, Ministry of Education, Southwest University of Science and Technology, Sichuan, Mianyang 621010, China
[d] CAS Center for Excellence in Comparative Planetology, Hefei 230026, China

ARTICLE INFO

*Keywords:*
Nuclear Waste
Iodate
Adsorption
Nanopore
Halloysite
Kaolinite

ABSTRACT

Naturally occurring porous minerals as adsorbents for the remediation of environmental pollution has been one of the hot topics in environmental science and material science. In this study, the adsorption of iodate ($IO_3^-$) on two nanosized tubular halloysite samples (HBHal and SCHal, from Hubei and Sichuan Province, China, respectively) were investigated for the first time. To evaluate the impact of nanopore of halloysite on the adsorption of $IO_3^-$, chemically similar platy kaolinite was used for comparative studies in the batch experiments. The adsorption of $IO_3^-$ on HBHal reached equilibrium within 36 h, and the adsorption kinetics and isotherm fitted the pseudo-second-order and Langmuir equation well, respectively. Both HBHal and SCHal exhibited high adsorption capability to $IO_3^-$, with distribution coefficients ($K_d$'s) of 131.6 ± 14.6 and 126.6 ± 3.1 mL/g, respectively, which were > 30 times higher than that for kaolinite (4.2 ± 2.3 mL/g). The specific surface area normalized $K_d$ values on halloysite samples were > 13.5-fold higher than that on kaolinite. In addition, halloysite had high selectivity to $IO_3^-$, and the adsorption capacities on the two halloysite samples were slightly affected by the concurrent anions, such as $SO_4^{2-}$, $NO_3^-$, or $ClO_3^-$. It was proposed that the curved octahedral sheet caused geometry match between three oxygen atoms in the iodate and three OH above the vacant site of the octahedral sheet. This work also gave insight into the potential application of halloysite on the adsorption of radioactive iodate in natural and engineering environments.

## 1. Introduction

Iodine is an essential element for human beings and animals, and deficiencies in environmental iodine can cause a number of health problems known as iodine deficiency disorder (IDD), such as goiter, cretinism or sterility (Longombe and Geelhoed, 1997). Understanding how iodine interacts with geologic materials is helpful for evaluating the availability of iodine to plant and the uptake of iodine by human through food chain (Nagata and Fukushi, 2010). In addition, radioactive iodines (such as $^{131}I$ and $^{129}I$) are the by-products of nuclear fission, and they have been released into soils and the atmosphere during the course of nuclear weapon tests, nuclear power plant operations, and nuclear accidents such as those occurred at Three Mile Island in the USA in 1979, at Chernobyl in Russia in 1986, and at Fukushima in Japan in 2011. The Fukushima Daiichi accident introduced $1.5 \times 10^7$ kg $^{131}I$ to the environment (Von Hippel, 2011), and $^{131}I$, with a radioactive half-life of eight days, accounted for much of the radiation during the first week after the release (Kaplan et al., 2014). Because of its long radioactive half-life (1.6 million years), $^{129}I$ is considered to be of strategic importance for the safety assessment of underground radioactive waste disposal. Study of iodine adsorption on geologic materials is also a necessary task to assess the long-term stability of disposed radioactive waste (Kaplan, 2003; Miller et al., 2015).

When natural organic matter is limited, in aqueous environments, iodine exists primarily as iodide ($I^-$) and iodate ($IO_3^-$) depending on redox conditions and pH (Fuge and Johnson, 2015). $IO_3^-$ is expected to exist under highly oxidized conditions across a wide pH range, and $I^-$ is more common in suboxic to reducing conditions with the entire pH range in the stability field of water (Fuge, 2013). Based on the underlying assumptions that $I^-$ is the primary species in natural water, most works focused on the adsorption of $I^-$ by geologic or synthesized materials such as natural minerals (Miller et al., 2015; Yu et al., 2019), soils (Dai et al., 2009), sediments (Kaplan et al., 2000), black carbon (Choung et al., 2013), layered double hydroxides (Iglesias et al., 2014)

* Corresponding author at: Department of Geoscience, University of Wisconsin–Madison, 1215 West Dayton Street, A352 Weeks Hall, Madison, WI 53706, United States.
*E-mail address:* hfxu@geology.wisc.edu (H. Xu).

https://doi.org/10.1016/j.clay.2019.105407
Received 26 September 2019; Received in revised form 12 November 2019; Accepted 8 December 2019

or some metal compounds (Liu et al., 2016). However, $IO_3^-$ occurs in surface waters and seawater and is stable with respect to $I^-$ in the presence of oxygen. Recent iodine speciation study reported that $IO_3^-$ is the predominant species and accounted for up to 84% of the total iodine present in groundwater samples recovered from the Hanford Site (Zhang et al., 2013). Therefore, the study of the adsorption behavior of $IO_3^-$ is as important as $I^-$ to predict the migration and fate of iodine and the remediation of radioactive iodine in natural environments.

Iron and aluminum oxides are regarded as important materials for $IO_3^-$ adsorption because of their high points of zero charge ($pH_{PZC}$). Dai et al. (2004) conducted batch adsorption experiments of $IO_3^-$ on 20 different soils from China, and the results showed that $IO_3^-$ adsorption was positively correlated with iron oxide contents. Couture and Seitz (1983) conducted adsorption experiments of $IO_3^-$ on hematite, and the results showed that $IO_3^-$ adsorption increased concomitantly with decreasing pH, which was typical behavior for anionic species adsorption on oxides. Nagata and Fukushi (2010) predicted the adsorption behaviors of $IO_3^-$ on oxides by surface complexation modeling and showed that the outer-sphere species were dominant for γ-$Al_2O_3$, whereas the inner-sphere species were dominant for hydrous ferric oxide and α-FeOOH. Another feature for $IO_3^-$ adsorption was that most minerals adsorb appreciably more $IO_3^-$ than $I^-$. For example, Ticknor and Cho (1990) reported that more $IO_3^-$ was adsorbed to fracture-filling minerals (chlorite, hematite, kaolinite, and goethite et al.) than $I^-$. The cause for the difference in $IO_3^-$ and $I^-$ adsorption behavior is presumably resulted from Lewis hard base nature of $IO_3^-$, as compared to $I^-$, which would favor interaction between Lewis hard base ($IO_3^-$) with Lewis hard acid sites on the mineral surface (Xu et al., 2017).

Clay minerals have been widely used in pollution control, but they were generally regarded as ineffective adsorbents to anions due to their inherent negative charge at most pH conditions (Xi et al., 2010). Thus, most works associated with the adsorption of anions by clay minerals focused on the surface or interlayer modification (Riebe et al., 2005; Matusik, 2014; Wei et al., 2019). Halloysite is a 1:1 dioctahedral phyllosilicate in kaolin group, which is a hydrated polymorph of kaolinite. Halloysite is chemically similar to kaolinite, but the unit layers of halloysite are separated by a monolayer of water molecules; accordingly, halloysite has a structural formula of $Al_2(OH)_4Si_2O_5{\cdot}nH_2O$ (Yuan et al., 2015; Deng et al., 2019). As a result, halloysite accommodates the mismatch between the smaller octahedral sheet and larger tetrahedral sheet via the wrapping of layers to form a nanosized tubular morphology (Bates et al., 1950). For kaolinite, the mismatch between the octahedral sheet and tetrahedral sheet is corrected via the rotation and distortion of the tetrahedral sheet to form a platy morphology (Tan et al., 2015). Generally, the length of halloysite nanotubes varies from submicrons to several microns and the external diameter varies from approximately 30 to 190 nm, with an internal nanotube diameter of ca. 10–100 nm (Yuan et al., 2008). The sizes of nanotubes vary in halloysite from different deposits (Pasbakhsh et al., 2013).

Unlike the other phyllosilicate minerals, the isomorphic substitutions in the kaolin group minerals are few (Bailey, 1988), thus the permanent negative charge are few for kaolin group minerals. In previous works, the adsorption of some oxyanions by kaolinite, such as $IO_3^-$ (Couture and Seitz, 1983), $NO_3^-$ (Xi et al., 2010), and $SO_4^-$ (Rao and Sridharan, 1984) were reported. Generally speaking, kaolinite showed low adsorption capacity to the oxyanions, in which the adsorption capacity of $IO_3^-$ was especially low (with a $K_d$ value of ~1.25 mL/g) (Couture and Seitz, 1983), likely due to the low charge and large molecular mass of iodate. With the special nanosized tubular morphology, the specific surface area and pore volume of halloysite are normally much higher than those of kaolinite, which are advantageous for contaminant adsorption. In addition, halloysite has multiple surface groups, external siloxane groups, interlayer inner-surface aluminol groups, and internal aluminol groups, which allow for diverse post-modification possibilities to improve the performance of halloysite as adsorbent for contaminants. Therefore, in the past decade, the use of halloysite or modified halloysite for applications in environmental remediation has received much attention (Yuan et al., 2015; Anastopoulos et al., 2018). However, to our knowledge, there have been no reports on the $IO_3^-$ adsorption behavior on halloysite so far.

In the present work, the adsorption of $IO_3^-$ on nanosized tubular halloysite was investigated for the first time. Kaolinite was also studied for comparison purposes. Attention was focused on the role of nanotubular morphology/nanopore in enhancing the adsorption of $IO_3^-$ on halloysite and on the possibility of exploiting halloysite as an adsorbent in the field of iodate remediation.

## 2. Materials and methods

### 2.1. Materials and chemicals

The non-radioactive iodine ($^{127}I$) was used in $IO_3^-$ uptake experiments. Potassium iodate ($KIO_3$) (Fisher Scientific Co., USA) was used as the source of $IO_3^-$. $K_2SO_4$ (AR Grade), $KNO_3$ (AR Grade), $KClO_3$ (AR Grade), NaOH (AR Grade) and 36.7% HCl were purchased from Fisher Scientific. Deionized water (resistivity, 18.2 MΩ·cm) was used in all of the experiments. All chemicals were used as received, without further purification.

Two raw halloysite samples were used for the study of iodate adsorption. They were collected from Danjiangkou, Hubei Province, China and Guangyuan, Sichuan Province, China, respectively. The samples were purified by repeated sedimentation processed to remove the quartz impurities, followed by drying at room temperature and grinding. The resultant samples are referred as HBHal and SCHal, respectively. A high-purity kaolinite sample (referred as Kaol) was from Murfreesboro, Arkansas, the USA.

### 2.2. Characterization methods

The X-ray diffraction (XRD) data were collected on a Rigaku Rapid II instrument (Mo $K\alpha$ radiation) with a two-dimensional (2D) image-plate detector in the Department of Geoscience at the University of Wisconsin–Madison. All the XRD patterns were collected at 50 kV and 50 mA using a 100-μm diameter beam collimator. The conventional $2\theta$ vs. intensity patterns were produced by converting the 2D images using the Rigaku's 2DP software.

The low-temperature nitrogen ($N_2$) adsorption-desorption isotherms were measured using an Autosorb-iQ2-MP gas adsorption analyzer (Quantachrome, Boynton Beach, FL) at liquid-nitrogen temperature. Prior to measurement, the samples were degassed at 150 °C for 12 h under vacuum. The total specific surface area of the samples, $S_{BET}$ was calculated from the nitrogen adsorption data using the multiple-point Brunauer-Emmett-Teller (BET) method (Brunauer et al., 1938), and the total pore volume, $V_{total}$, was evaluated based on $N_2$ uptake at a relative pressure of approximately 0.99. The Barrett-Joyner-Halenda (BJH) method (Barrett et al., 1951) was used to calculate the pore size distribution (PSD) from the adsorption branch of the isotherms.

Transmission electron microscopy (TEM) experiments were conducted using a Tecnai T12 with a 120 kV acceleration voltage. The specimens were prepared by the following procedure: the clay mineral samples were ultrasonically dispersed in ethanol for 5 min, and a droplet of the sample suspension was then dropped onto a lacy carbon-coated 200-mesh Cu grid which was left to stand for at least 10 min before being transferred into the microscope.

The point of zero net proton charge (PZNPC) and surface site density ($D_s$) analyses were conducted by acid-base titration method using a Mettler Toledo DL50 Graphix titrator. The HCl (0.1 mol/L) and NaOH (0.1 mol/L) solutions were used as titrants with concentrations calibrated by sodium carbonate and potassium hydrogen phthalate, respectively. The titration was carried out by placing 0.25 g clay mineral samples with 50 mL deionized water in a 100 mL titration cup at 25 °C. Initially, the pH value of suspensions was quickly lowered to

approximately 2.2 by 5 mL HCl. After 10 min of equilibrium, the suspensions were slowly back-titrated using an end point titration (EP) method with NaOH until pH reached 10. Each step was allowed to stabilize until the pH drift was < 0.005 pH unit per min.

### 2.3. Iodate adsorption and desorption experiments

Batch experiments of $IO_3^-$ adsorption were carried out by shaking 0.1 g dry samples with 20 mL of $IO_3^-$ solutions in a 50 mL centrifuge tube fitted with a cap at 25 °C. The $IO_3^-$ solution was prepared by dissolving $KIO_3$ in deionized water. The initial pH and final pH were measured using a pH meter (Accumet XL20, Fisher Scientific). For the kinetics tests, the initial concentration of $IO_3^-$ in the solution was 0.1 mmol/L (mM), and the mixture in the centrifuge tubes was strongly shaken at a rate of 150 rpm in a platform shaker. The adsorption time was in the range from 1 to 72 h. At the end of each time intervals, the suspensions were centrifuged at 4000 rpm for 10 min, and then the supernatants were removed with a pipette and refrigerated for $IO_3^-$ concentrations analysis. A Dionex 1000 Ion Chromatography (IC) with an AS22 guard and analytical column was used to measure $IO_3^-$ concentrations, with a 5.4 mM $Na_2CO_3$/1.68 mM $NaHCO_3$ solution as the eluent.

The experiments for the comparison adsorption of the three samples (HBHal, SCHal, and Kaol) followed a procedure very similar to the kinetics experiments except for the shaken time is 48 h as determined from the kinetics experiment (see following). The pH values of the suspensions in the comparison experiments were not deliberately adjusted and were measured at the end of the 48 h mixing period, and the final pH values are listed in Table 1. To study the effect of pH on the adsorption of $IO_3^-$, the pH values of the suspensions were adjusted approximately to 5.0, 6.5, and 7.8, respectively by incrementally adding 0.1 M NaOH or 0.1 M HCl. The NaOH and HCl were added every 12 h until the desired pH was obtained during a 48-h period. The adsorption isotherm was obtained according to a very similar procedure, and the initial concentrations of $IO_3^-$ in the solutions were 0.01, 0.02, 0.05, 0.1, 0.2, 0.5, and 1 mM, respectively. The competitive adsorption experiments also followed a procedure similar to the comparison adsorption experiments, but using a pre-prepared two-component solution instead of the iodate solution. The composition of the two-component was 0.1 mM $IO_3^-$ and 1 mM another anion ($SO_4^{2-}$/$NO_3^-$/$ClO_3^-$). Each adsorption point was the average of duplicate or triplicate experiments. Blank experiments confirmed the absence of wall adsorption or $IO_3^-$ loss to volatilization.

Solid: liquid partitioning coefficient ($K_d$, mL/g) was calculated using the following equation:

$$K_d = (C_0 - C_t)/(C_t \times S) \quad (1)$$

where $C_0$ and $C_t$ (mM) are the concentration of $IO_3^-$ in the reaction solution before and after adsorption for time $t$ (h), respectively. $S$ is the solid:solution ratio (g/mL). The amount of $IO_3^-$ adsorbed per unit mass of the adsorbent, $q_t$ (mg/g) was calculated as:

**Table 1**
Porous parameters, PZNPC[a], and surface site densities of samples.

| Samples | $S_{BET}$ ($m^2$/g) | $V_{total}$ (cc/g) | PZNPC[a] | $H_s$[b] ($10^{-4}$ mol/L) | $D_s$[c] (sites/$nm^2$) | pH[d] |
|---|---|---|---|---|---|---|
| HBHal | 54.2 | 0.3503 | 9.1 | 3.39 | 0.75 | 6.43 |
| SCHal | 68.2 | 0.3843 | 7.8 | 3.34 | 0.58 | 6.37 |
| Kaol | 29.8 | 0.2534 | 6.2 | 3.69 | 1.48 | 4.90 |

[a] The point of zero net proton charge.
[b] The maximum surface proton bond site concentration.
[c] The surface site density.
[d] The final pH values for the comparison adsorption experiments of the three samples.

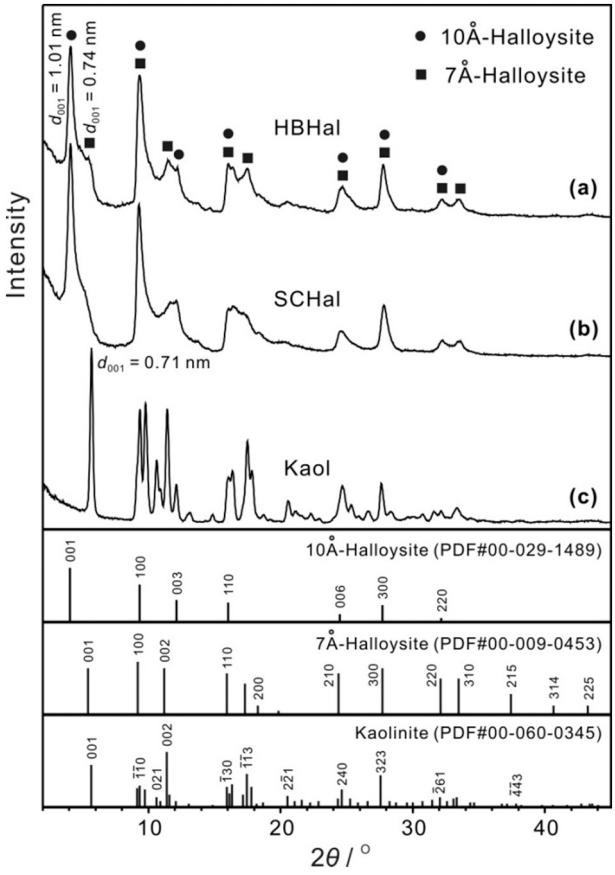


**Fig. 1.** XRD patterns (Mo $K\alpha$) of halloysite and kaolinite samples: (a) HBHal, (b) SCHal, and (c) Kaol.

$$q_t = (C_0 - C_t) \times M/m \quad (2)$$

where M is the molar mass of $IO_3^-$, and $m$ (g) is the amount of adsorbent in 1 L of iodate-bearing solution.

After adsorption experiments, the solid samples were collected by centrifugation. 0.1 $g$ solid samples with pre-adsorbed $IO_3^-$ were sequentially exposed to 20 mL water, shaking on a platform shaker (150 rpm) for 1 to 48 h. The amounts of $IO_3^-$ desorbed from each sample were then calculated based on the concentration of $IO_3^-$ in the desorption solutions, $C_{d(t)}$ (mM). The desorption mass percentage (%) was calculated using the equation:

$$\text{Desorption (\%)} = [C_{d(t)}/(C_0 - C_F)] \times 10 \quad (3)$$

where, $C_F$ (mM) is the concentration of $IO_3^-$ in the reaction solution after adsorption.

## 3. Results and discussion

### 3.1. Characterization of samples

The XRD patterns of the samples are shown in Fig. 1. It can be seen from the XRD patterns of HBHal and SCHal that they were dominated by 10 Å-halloysite, with the 001 reflection at 1.01 nm ($d$ value) (Fig. 1a and b). HBHal and SCHal also contained minor portion of 7 Å-halloysite, indicated by the (001) reflection at 0.74 nm. The 7 Å-halloysite is resulted from dehydration of 10 Å-halloysite at room temperature, as the interlayer water is weakly held and easily removed (Yuan et al., 2008). These results indicated that there were halloysite samples in both fully hydrated and dehydrated states in HBHal and SCHal. The 10 Å-halloysite could be kept fully hydrated only by keeping the sample in a sealed container in contact with water or a water-saturated atmosphere. The kaolinite sample was of high purity and well ordered, as

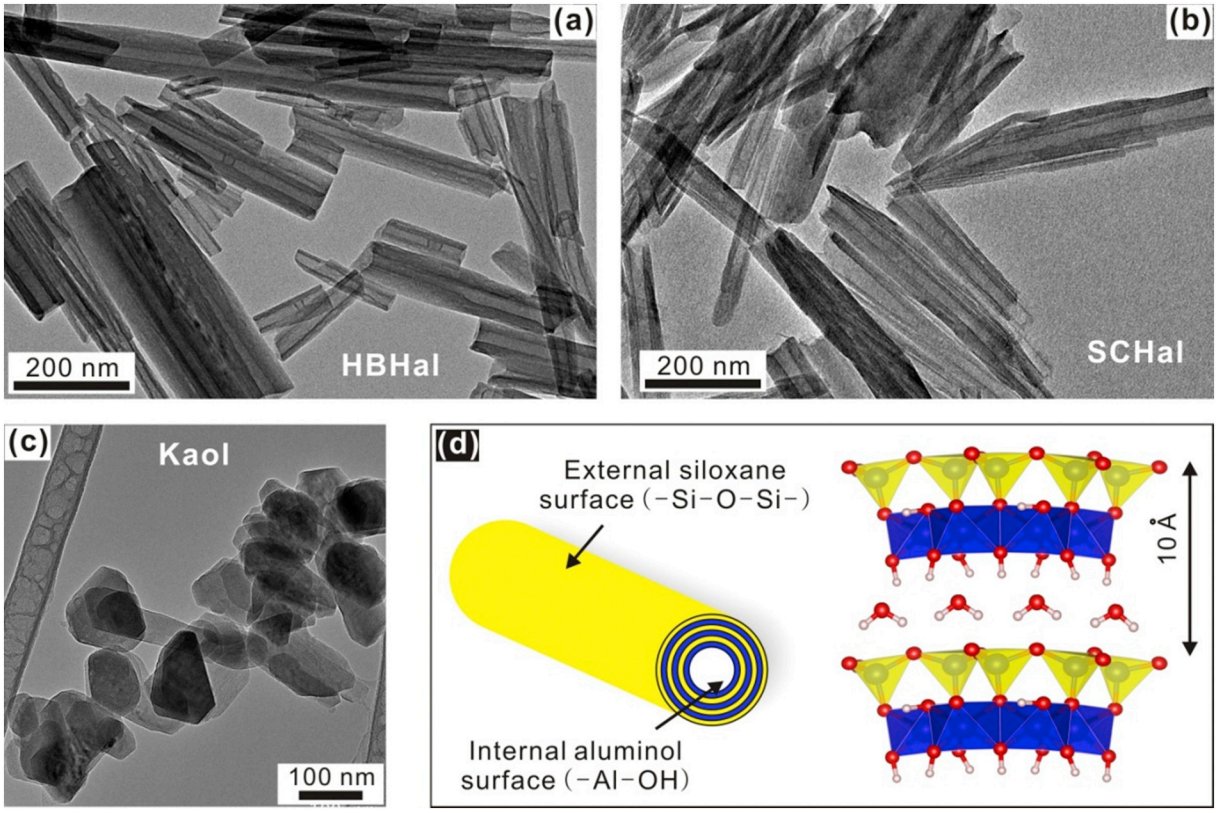


**Fig. 2.** TEM images of halloysite and kaolinite samples: (a) HBHal; (b) SCHal; (c) Kaol. (d) A schematic illustration of crystalline structure of halloysite nanotube (Joussein et al., 2005; Yuan et al., 2015).

revealed by sharp diffraction peaks, with a characteristic $d_{001}$ value of 0.71 nm (Fig. 1c).

The TEM images illustrated in Fig. 2a and b showed that the halloysite particles had a cylindrical shape and contain a transparent central area that runs longitudinally along the cylinder, indicating that the halloysite particles were hollow and open-ended. As measured statistically from several TEM images, the length of individual nanotubes of HBHal was ~0.2–1.0 μm, the external diameter of HBHal nanotubes ranged from approximately 40 to 65 nm, and the internal diameter of HBHal nanotubes varied from approximately 12 to 22 nm; the length of individual nanotubes of SCHal was ~0.3–1.0 μm, the external diameter of SCHal nanotubes ranged from approximately 40 to 84 nm, and the internal diameter of SCHal nanotubes varied from 10 to 28 nm. HBHal was more uniform in the external and internal diameters of nanotubes than SCHal. It is noteworthy that the accuracy of these dimensions is limited by the small number of particles observed in the TEM images. The Kaol sample displays platy particles with typical pseudo-hexagonal morphology, with a particle size of about 100–300 nm (Fig. 2c). Fig. 2d shows the schematic representation of a halloysite nanotube and the crystalline structure of 10 Å-halloysite. In each halloysite nanotube, the external surface was composed of siloxane (Si-O-Si) groups, whereas the internal surface consisted of a gibbsite-like array of aluminol (Al-OH) groups (Joussein et al., 2005; Yuan et al., 2015).

The nitrogen adsorption-desorption isotherms of the two halloysite samples (HBHal and SCHal) belonged to the type IV with H3 hysteresis loops (Fig. 3a), according to IUPAC classification (Gregg et al., 1982). This type of isotherm was a typical characteristic of mesoporous structures. The hysteresis was associated with the filling and emptying of the mesopores by capillary condensation. The isotherm of Kaol characterized as a type II isotherm with an H3 hysteresis loop (Fig. 3a). The hysteresis loop indicated the existence of mesopores in Kaol, which resulting from packing of kaolinite particles. It could be found from Table 1, the $S_{BET}$ and $V_{total}$ of HBHal and SCHal were larger than those of Kaol, attributed to the thinner clay platelets of halloysite and the hollow nanotubular morphology of halloysite. The $S_{BET}$ of Kaol is 29.8 $m^2/g$, which is appreciably larger than the usual specific surface area of kaolinite (10–20 $m^2/g$) reported in the literature (Castellano et al., 2010), due to its small particle size of the kaolinite.

The PSD curve of HBHal shows two distinct mesopore populations centered at approximately 2.3 nm and 15.5 nm, respectively (Fig. 3b). The mesopore population centered at 2.3 nm can be ascribed to pores that were newly formed during the degas process, in which the dehydration of tubular halloysite occurred. Kohyama et al. (1978) reported that the rolled layers of tubular halloysite, which were originally tightly connected in the fully hydrated mineral, become separated from each other and created slit-shaped longitudinal pores with several nanometers wide after the dehydration of halloysite. The mesopore population centered at 15.5 nm is identified as the lumen of HBHal. SCHal exhibited a similar PSD curve to HBHal, but the pore population centered at 15.6 nm assigned to the lumen of SCHal is broader than that for HBHal (Fig. 3b). This result indicated the irregularity in the internal diameter of SCHal nanotubes, which is consistent with the results of TEM (Fig. 2b). The broad pore population in the range of 10–60 nm for Kaol is attributed to the disordered staking of kaolinite particles. This nitrogen adsorption-desorption results clearly complemented TEM results and provides a more integrated understanding of porosity of the samples, because it is more representative of the entire sample.

Fig. 4a shows the acid-base titration results of the samples. $H_t$ is the total proton concentration (Nie et al., 2013) and defined as:

$$H_t = [H^+] - [OH^-] + [\equiv SOH_2^+] - [\equiv SO^-] \quad (4)$$

where, $[H^+]$ and $[OH^-]$ are the concentration of protons and hydroxide ions in solution, respectively. $[\equiv SOH_2^+]$ and $[\equiv SO^-]$ are the surface species derived from protonation and deprotonation reactions of surface hydroxyl groups (Eqs. (5) and (6)), respectively.

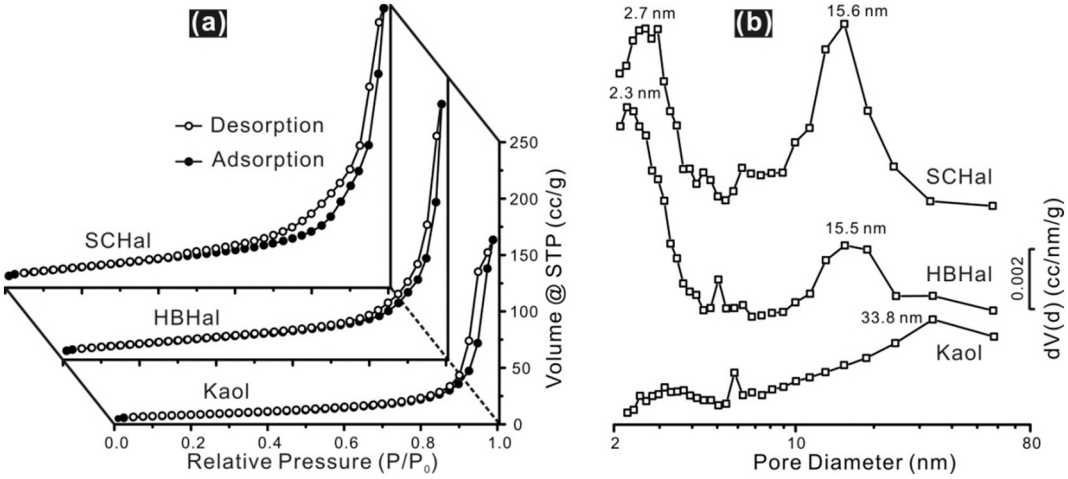


**Fig. 3.** (a) Nitrogen adsorption-desorption isotherms and (b) pore size distribution (PSD) curves of samples.

$$\equiv SOH + H^+ = \equiv SOH_2^+ \quad (5)$$

$$\equiv SOH = \equiv SO^- + H^+ \quad (6)$$

$H_t$ was calculated from the following equation:

$$H_t = (C_a V_a - C_b V_b)/(V_0 + V_a + V_b) \quad (7)$$

where $C_a$ and $C_b$ are the calibrated concentrations of HCl and NaOH, mol/L; $V_0$, $V_a$, and $V_b$ are the volumes of the initial suspension and the consumed volumes of HCl and NaOH solution, respectively, L.

The point of zero net proton charge (PZNPC) of minerals is the pH at which the surface proton charge is zero (i.e. $[\equiv SOH_2^+] = [\equiv SO^-]$). In a system where protons and hydroxide ions are the only aqueous species, PZNPC is the pH at which the positively and negatively charged functional groups are equal (Drever and Marion, 1998). Ascertaining the PZNPC of minerals is useful in predicting its electrostatic interaction with charged aqueous species. In this work, the PZNPC was calculated by the difference between the number of protons added during the titration (i.e. $H_t$) and the number of protons remaining in solution (Hao et al., 2018), and the PZNPC results of halloysite and kaolinite are listed in Table 1. The PZNPC of Kaol is 6.2 (Table 1), which is falling in the reported PZNPC range (from 3.0 to above 7) of kaolinite in the literature (Schroth and Sposito, 1997). The disagreement can be attributed to differences in the origin of kaolinite and to the different experiment conditions. The PZNPC values of the two halloysite samples are higher than that of Kaol (Table 1). Two reasons may attribute to the higher PZNPC values of halloysite: more isomorphic substitutions (such as the replacement of Si(IV) by Al(III) in the tetrahedral layer) existed in halloysite (Tarı et al., 1999), in comparison with kaolinite, which created more permanent negatively charged sites in halloysite, resulting in higher PZNPC (Stumm, 1992); the nanoscale pore space confinement may also cause an increase in the PZNPC of halloysite, due to the deviation of surface chemistry of aluminol groups in the nanopores (Wang et al., 2002). Generally, the breadth of the distribution of PZNPC values of clay minerals is much larger than what is typical for oxide minerals. For example, the PZNPC of $\gamma$-$Al_2O_3$ is 8.5 ± 0.2, based on the data compiled by Goldberg et al. (1996).

The surface site density of samples was determined by the Gran function (Eqs. (8) and (9)) (Liang et al., 2017):

$$\text{Gran} = (V_0 + V_a + V_b) \times 10^{-pH}, \text{ for pH} < 7.0 \quad (8)$$

$$\text{Gran} = (V_0 + V_a + V_b) \times 10^{(pH + \log Kw)}, \text{ for pH} > 7.0 \quad (9)$$

where, $V_0$, $V_a$, and $V_b$ are the same as those in Eq. (7), Kw is the ionic product of water at a given temperature, and in this work, *log*Kw is considered to be −13.93 with the temperature of 25 °C (Bujňáková et al., 2013). The plot of Gran's function versus the added volume of titrant was fit with two lines that cross the X-axis at $V_{eb1}$ and $V_{eb2}$. The titration results of the samples are presented in Fig. 4b as a function of the added volume of NaOH solution. The maximum surface proton bond site concentration, $H_s$ (mol/L), during the titration was calculated by Eq. (10):

$$H_s = [(V_{eb2} - V_{eb1})C_b - (V_{2-blank} - V_{1-blank})C_b]/V_0 \quad (10)$$

Then, the surface site density, $D_s$ (site/nm$^2$) can be calculated by Eq.

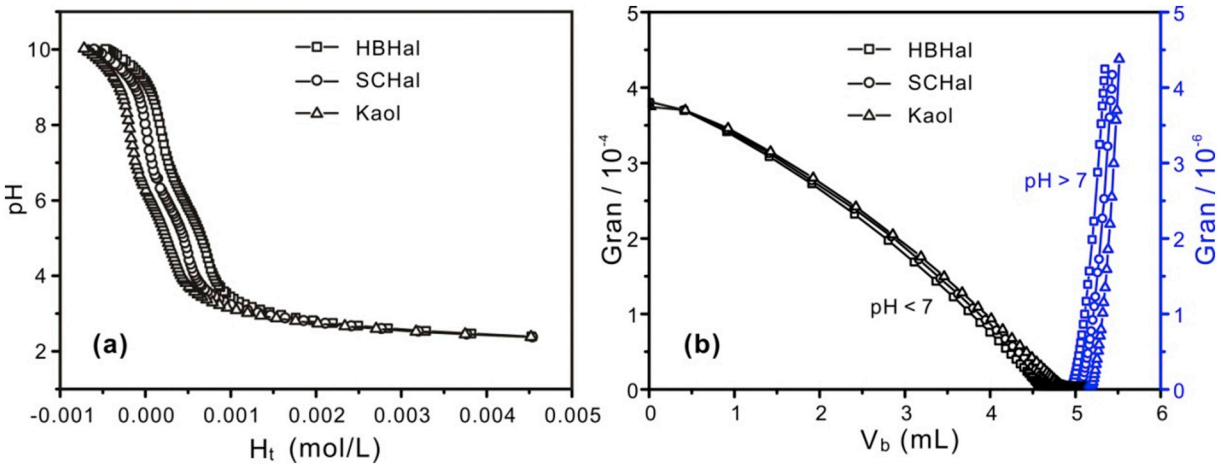


**Fig. 4.** (a) Acid-base titration curves of samples in deionized water and (b) Gran's plots to obtain $V_{eb1}$ and $V_{eb2}$ (see text for notation).

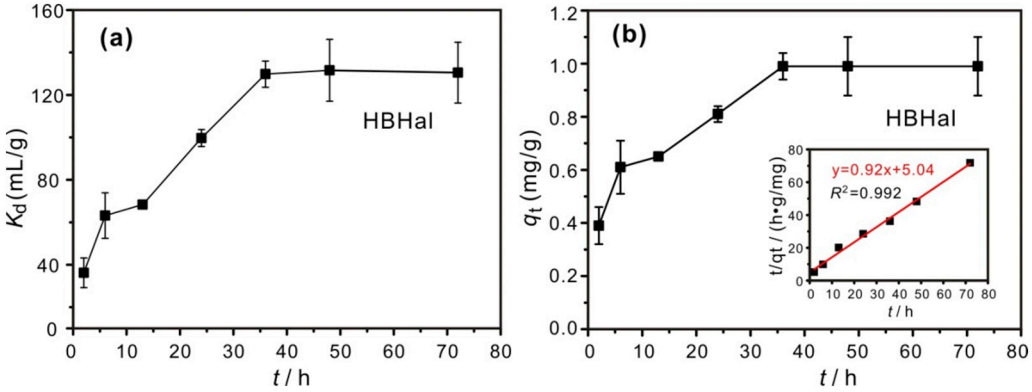


**Fig. 5.** (a) Iodate-$K_d$ values as a function of adsorption time and (b) adsorption kinetics of $IO_3^-$ on HBHal (inset is the linear fitting plot based on pseudo-second-order kinetic model), pH ≈ 6.4.

(11):

$$D_s = H_s N_A / S_{BET} C_s 10^{18} \quad (11)$$

where, $N_A$ is Avogadro's constant, 6.02 × $10^{23}$ $mol^{-1}$; $S_{BET}$ is the specific surface area of samples, $m^2/g$; and $C_s$ is the sample dosage, g/L.

As shown in Table 1, the $D_s$ value for Kaol is 1.48 sites/$nm^2$, which is in the same order of magnitude with the reported result (0.6 sites/$nm^2$) from crystallographic data computed by Sposito (1984). Riese (1982) reported a $D_s$ value of 6 sites/$nm^2$ for kaolinite KGa-1 determined by tritium exchange, but Westall and Hohl (1980) pointed out the number of surface sites available by acid/base titration is only ~10% of that determined by tritium exchange. The $D_s$ values for HBHal and SCHal are slightly smaller than that for Kaol (Table 1). This difference can be explained by a greater percentage of edge area due to the platy morphology of the kaolinite.

### 3.2. Performance of samples for iodate adsorption

$IO_3^-$ adsorption on HBHal was investigated as a function of adsorption time to establish the equilibrium time of adsorption. It can be found from Fig. 5a the $K_d$ values increase with the adsorption time, and the adsorption of $IO_3^-$ on HBHal reaches equilibrium within 36 h. The reason for the increases of $K_d$ values with adsorption time in the early stage may be attributed to diffusion limitations of the $IO_3^-$ to the adsorption sites. The extended adsorption time would allow more $IO_3^-$ to diffuse into the halloysite lumen, thereby permitting $IO_3^-$ to come into contact with additional adsorption sites. From the TEM and nitrogen adsorption-desorption results, HBHal had the smallest pore size, so it could be expected that HBHal would take the longest time to reach the adsorption equilibrium. A period of 48 h was used as the adsorption time for the following experiments to ensure that adsorption equilibrium was reached.

The kinetics curve of the adsorption process of HBHal is fitted using the pseudo-second-order model (Liu et al., 2012), with the rate expression given by:

$$dq_t/dt = k(q_e - q_t^2) \quad (12)$$

where $k$ is the pseudo-second-order rate constant (g/mg·h), $q_t$ (mg/g) is the amount of $IO_3^-$ adsorbed per unit mass of adsorbent at time $t$ (h), and $q_e$ (mg/g) is the equilibrium adsorption capacity. Eq. (12) can be rearranged to obtain the linear form:

$$t/q_t = 1/(kq_e^2) + t/q_e, \quad (13)$$

where $kq_e^2 = h$, and $h$ is the initial adsorption rate (mg/(g·h)). As shown in Fig. 5b and Table 2, which provide the fitting results, the adsorption of $IO_3^-$ on HBHal fits Eq. (13) well. This result indicates that the kinetics of this adsorption system is classified as pseudo-second-order (Limousin et al., 2007).

**Table 2**
Kinetics constants and Langmuir equation parameters for iodate adsorption on HBHal.

| Kinetics constants | | Langmuir parameters | |
|---|---|---|---|
| $k$ (g/mg·h) | 0.17 | $b$ (L/mmol) | 5.82 |
| $h$ [mg/(g·h)] | 0.20 | $Q_m$ (mg/g) | 3.90 |
| $q_e$ (mg/g) | 1.09 | $R_L$ | 0.15–0.95 |
| $R^2$ | 0.992 | $R^2$ | 0.975 |

Fig. 6a shows the results of the comparison adsorption of $IO_3^-$ on HBHal, SCHal, and Kaol. The $K_d$ values for HBHal and SCHal are 131.6 ± 14.6 and 126.6 ± 3.1 mL/g, respectively, which are > 30 times higher than that for Kaol (4.2 ± 2.3 mL/g) (Fig. 6a). The low $K_d$ value for Kaol is consistent with the previous report that kaolinite is a very weak adsorbent for $IO_3^-$ (Couture and Seitz, 1983). The higher $K_d$ values for halloysite samples cannot be fully explained by their higher specific surface area (Table 1), because the specific surface area normalized $K_d$ ($K_{d\text{-}s}$) values for the two halloysite samples are also significantly larger than that for Kaol (Fig. 6a). The $K_{d\text{-}s}$ values for HBHal and SCHal samples are > 13.5 times larger than that for kaolinite. This significant enhancement in the adsorption capacity to $IO_3^-$ for halloysite over kaolinite should be attributed to the effects of nanopore in halloysite.

Fig. 6b and c show the $IO_3^-$ adsorption as a function of pH. As the pH of the system decreased below 7.8, the amount of $IO_3^-$ adsorption ($K_d$ and $K_{d\text{-}s}$) on halloysite increased concomitantly with decreasing pH. Considering the PZNPC of the two halloysite samples are higher than 7.8 (Table 1), the decreasing pH resulted in a greater extent of protonation of inner surface aluminol groups and thus more positive charges on the inner surface of the nanotubes. The influence of pH on the adsorption capacity suggests that the electrostatic attraction between $IO_3^-$ and protonated aluminol surface constitutes an important driving force of the adsorption process. At pH approximately 5, a decrease of the amount of $IO_3^-$ adsorption was observed (Fig. 6b and c), due to the dissolution of Al octahedral sheet under acid condition (Zhang et al., 2012). It is noteworthy that under the neutral to weakly alkaline pH conditions, which are the typical pH ranges of groundwater, halloysite shows high adsorption capacity to $IO_3^-$, but kaolinite shows little or no $IO_3^-$ adsorption. The higher $K_{d\text{-}s}$ values for HBHal than those for SCHal (Fig. 6c) are attributed to the higher surface site densities of HBHal (Table 1).

HBHal was used to test the adsorption isotherms of $IO_3^-$ on halloysite. Fig. 6b displays the $IO_3^-$ adsorption isotherm of HBHal. The Langmuir adsorption isotherm model demonstrated the best fit for quantitatively describing the adsorption data compared with several commonly used fitting models, such as the Freundlich and Redlich-Peterson models (Limousin et al., 2007). The Langmuir model is

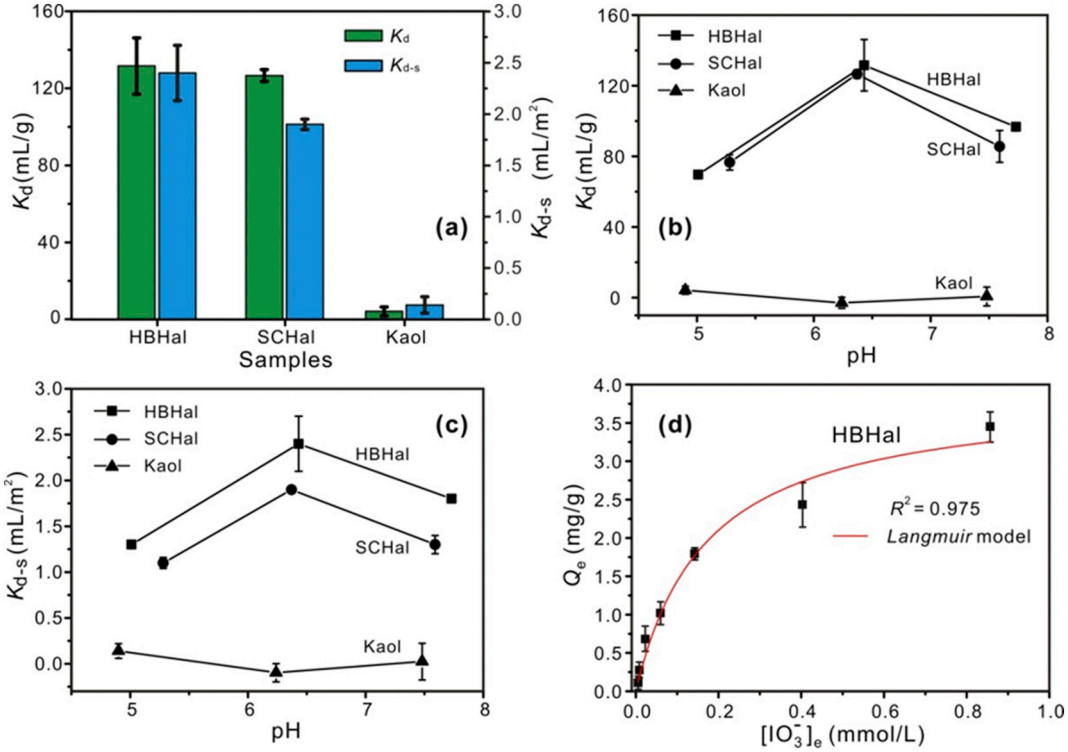


**Fig. 6.** (a) Iodate-$K_d$ and iodate-$K_{d-s}$ values for different samples; (b) and (c) effect of pH on the $IO_3^-$ adsorption on different samples; (d) the $IO_3^-$ adsorption isotherm of HBHal, pH = 6.4 ± 0.1.

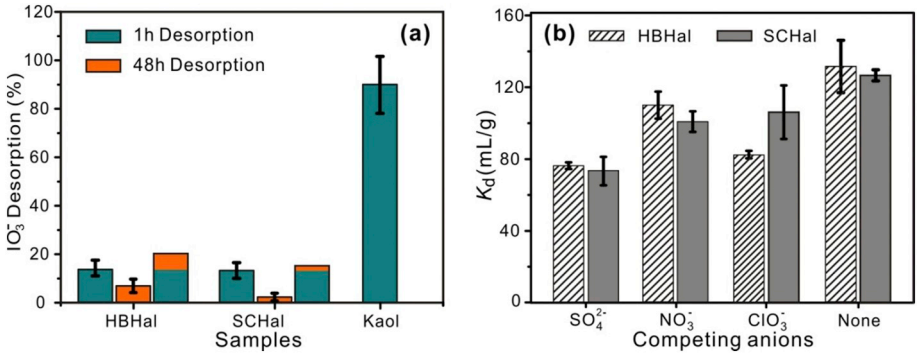


**Fig. 7.** (a) Percentage of $IO_3^-$ desorption by sequential extraction of samples pre-adsorbed $IO_3^-$ by deionized water for 1 h and 48 h; (b) Iodate-$K_d$ values of HBHal and SCHal when $IO_3^-$ (0.1 mM) coexisted with $SO_4^{2-}$ (1 mM), $NO_3^-$ (1 mM), and $ClO_3^-$ (1 mM), respectively. None means the $K_d$ values of HBHal and SCHal without competing anions.

described by the following equation (Yuan et al., 2013):

$$Q_e = Q_m bC_e/(1 + bC_e) \quad (14)$$

where $Q_e$ (mg/g) is the amount of adsorbed $IO_3^-$ at equilibrium concentration $C_e$ (mM), $Q_m$ (mg/g) and $b$ are the Langmuir adsorption capacity and Langmuir constant, respectively.

The adsorption coefficients computed from Eq. (14) are summarized in Table 2. The Langmuir adsorption capacity of HBHal is 3.90 mg/g (Table 2). Here, assuming a mono-dentate $IO_3^-$ complex formed on the surface of HBHal (i.e. surface sites and adsorbate occur in a 1:1 ratio response), the reactive adsorption sites at the HBHal surface calculated from the Langmuir adsorption capacity is 0.25 sites/nm$^2$. The available surface sites as determined by titration (Table 1) remained in 3-fold excess to the maximum $IO_3^-$ values all cases. The specific conformation of $IO_3^-$ with the surface hydroxyl groups of HBHal will be investigated by X-ray absorption spectroscopic studies in future. It is noteworthy that the Langmuir adsorption capacity of HBHal is 17.6 times higher than that of Perudic Ferrisols soil samples from Hainan Province, China (Dai et al., 2004), about one seventh of that of organoclay (Li et al., 2018), and one tenth of that of activated carbon Filtrsorb 400 (with a BET surface area of 1050 m$^2$/g) (Mahmudov and Huang, 2011). These results indicated that halloysite exhibited very high Langmuir adsorption capacity to $IO_3^-$, which may make it a promising candidate for adsorption of $IO_3^-$.

In the Langmuir adsorption isotherm model, the separation factor, $R_L$, is often used to evaluate the affinity between the adsorbent and adsorbate. $R_L$ is defined by the following equation:

$$R_L = 1/(1 + bC_0) \quad (15)$$

where $C_0$ is the initial concentration (mM) of $IO_3^-$ and b is the Langmuir constant. According to the value of $R_L$, different affinities between the adsorbent and adsorbate are classified as follows: favorable adsorption ($0 < R_L < 1$), linear adsorption ($R_L = 1$), and unfavorable adsorption ($R_L > 1$) (Weber and Chakravorti, 1974). From Table 2, the $R_L$ value of HBHal is in the ranges of 0–1, indicating the favorable uptake of $IO_3^-$ by halloysite.

The results of desorption experiments of samples with pre-adsorbed $IO_3^-$ are shown in Fig. 7a. 14.3% and 13.4% of pre-adsorbed $IO_3^-$ were desorbed from HBHal and SCHal, respectively, after exposure to deionized water for 1 h, probably due to the release of weakly adsorbed $IO_3^-$ on the external surface and/or edge surface of halloysite. In contrast, 90.1% of preadsorbed $IO_3^-$ was mobilized from Kaol after

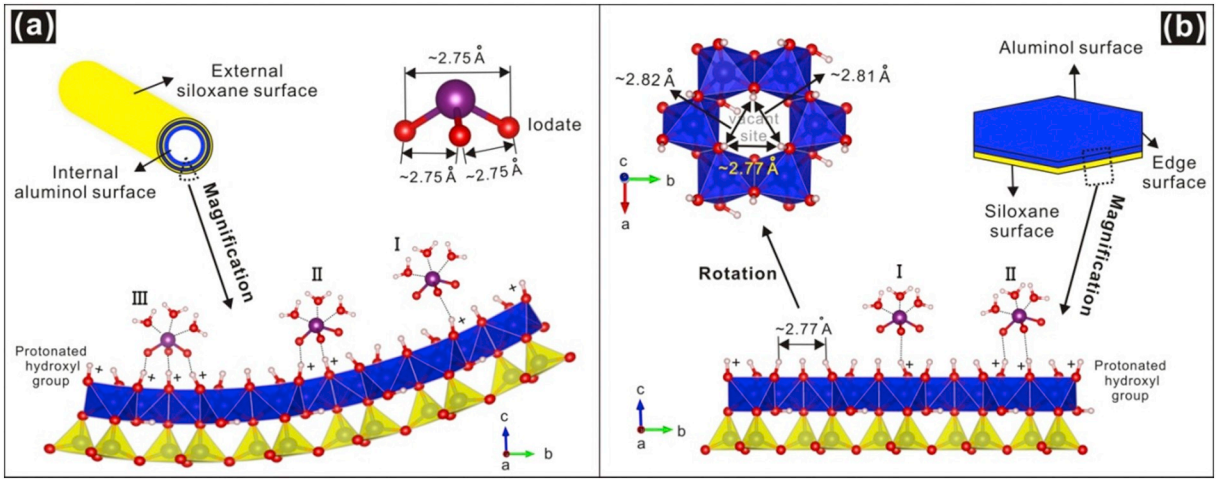


**Fig. 8.** Schematic presentation for the related mechanism of adsorption of $IO_3^-$: (a) on halloysite and (b) on kaolinite.

exposure to deionized water for 1 h, indicating the interaction between kaolinite and adsorbed $IO_3^-$ is very weak. Extending the time of desorption to 48 h resulted in 7.9% and 2.2% more of $IO_3^-$ release, total of 22.2% and 15.6% of $IO_3^-$ were released from HBHal and SCHal, respectively. The remaining 77.8% and 84.4% of $IO_3^-$ in HBHal and SCHal, respectively, may be strongly bonded by the internal surface of halloysite nanotubes. This result indicated that halloysite exhibited much stronger adsorption to $IO_3^-$ than kaolinite, due to the nanotubular morphology of halloysite.

In the actual environment, $IO_3^-$ may coexist with other anions. For example, a groundwater sample collected from the Hanford Site contained 1.13 mM sulfate ($SO_4^{2-}$) (Kaplan et al., 2000). Therefore, $SO_4^{2-}$, $NO_3^-$, and $ClO_3^-$, respectively, were used to study the concurrent adsorption with $IO_3^-$ on halloysite. As shown in Fig. 7b, the $K_d$ values of both HBHal and SCHal decreased slightly when another anion coexisted with $IO_3^-$ in the solution. The $K_d$ values decreased most when $SO_4^{2-}$ coexisted with $IO_3^-$, and the $K_d$ values decreased slightly as the coexisted anion was $NO_3^-$ or $ClO_3^-$. This result was probably due to the higher charge of $SO_4^{2-}$ than $NO_3^-$ and $ClO_3^-$. It is noteworthy that the concentration of the concurrent anions was 1 mM, which was 10 times higher than that of $IO_3^-$ in the solution, but all the $K_d$ values of the two halloysite samples were larger than 72.7 mL/g (Fig. 7b). This result suggested that halloysite had high selectivity to $IO_3^-$ and that a large proportion of adsorbed $IO_3^-$ was not affected by the concurrent anions.

### 3.3. Adsorption mechanisms and implications for iodate geochemistry

The adsorption of ions on kaolin group minerals can be explained by two mechanisms (Matusik, 2016). The first, involving the ion exchange, is related to permanently charged sites present at particle faces, which is caused by isomorphic substitutions in the mineral structure. The permanent charge is always negative for kaolinite and halloysite, arising from Si(IV) substitution by Al(III) in the tetrahedral sheet, Al(III) substitution by Fe(II) in the octahedral sheet or both. It was known that the isomorphic substitutions in the kaolin group minerals were very minor (Bailey, 1988). The substitution in halloysite usually did not exceed ~1% (Joussein et al., 2005), and less isomorphic substitution was reported in kaolinite (Tarı et al., 1999). So this mechanism is not significant in the adsorption process, and in this study, this mechanism can be excluded because the negatively charged site cannot be a reactive site for anions. The second mechanism is connected with the pH-dependent charge and involves surface complexation. The nature of pH-dependent charge is strongly affected by the pH of the solution in which the minerals are dispersed. Under acidic or alkaline conditions the surface hydroxyl groups may undergo protonation or deprotonation (Eqs. (5) and (6)) which induces positively or negatively charged sites, respectively.

The current adsorption conditions, pH values, are below the points of zero proton charge of the two halloysite samples (Table 1). As a result, the positively charged sites are expected on the surface of the samples, and the electrostatic interactions could lead to the adsorption of free $IO_3^-$ onto the samples. The surface complexation between $IO_3^-$ and the surface hydroxyl of this two minerals is expected to be the primary adsorption mechanism in this study, and the detailed conformation of $IO_3^-$ with the samples will be studied in the future work.

As shown by the adsorption results (Figs. 6a), halloysite exhibited a higher adsorption capability to $IO_3^-$, compared to kaolinite, and a > 12.5-fold increase in the surface area normalized $K_d$ value on halloysite was found. In addition, halloysite exhibited a stronger adsorption to $IO_3^-$ than kaolinite, concluded from the desorption results (Fig. 7a). With the similar chemical composition of the two minerals, this enhancement in the adsorption capability and adsorption interaction to $IO_3^-$ on halloysite should attribute to the nanosized porous structure of halloysite. As shown in Fig. 8a, iodate has a trigonal pyramidal molecular geometry with the oxygen atoms distances of ~2.75 Å (Fig. 8a) (Ghose and Wan, 1978). The three oxygen atoms are weakly negatively charged, because the electrons are delocalized in the structure of iodate. For kaolinite, the distances between the three H atoms above the vacant site of the octahedral sheet are ~2.77 Å, ~2.81 Å, and ~2.82 Å (Fig. 8b) refined by Bish (1993). It is noteworthy that the structure of Bish was based on data collected at 1.5 K (Bish, 1993), and that the distances between the three H atoms should be slightly larger at room temperature, which is larger than the size of iodate. The possible adsorption models for kaolinite include the protonated octahedral surface interaction with iodate via one (type I in Fig. 8b) or two oxygen atoms (type II in Fig. 8b) of iodate due to the molecular size. These two type adsorption are very weak due to the weak charge of the oxygen atoms and the large molecular mass of iodate. As for halloysite, the curvature of the structural layer caused a decrease in the distance between H atoms of octahedral sheet above the vacant site, which might cause geometry match between three oxygen atoms in iodate (Fig. 8a) and three OH above the vacant site of the octahedral sheet (Fig. 8b), forming a strong adsorption via three oxygen atoms interaction (type III in Fig. 8a). This size match hypothesis was supported by the result that halloysite had high selectivity to iodate (Fig. 7b).

In addition, it was reported that the properties of water in the nanopores deviated significantly from those of bulk water, such as the density, surface tension, and dielectric constant of water in nanopores were smaller than those of bulk water (Levinger, 2002; Wang et al., 2002). In this study, it is possible that the decrease in dielectric constant

of water could increase the propensity of $IO_3^-$ to lose its hydration sphere and form more strong inner-sphere complexes in the nanopore of halloysite (Knight et al., 2018). Wang et al. (2002) reported an increase in surface charge density of nanoporous alumina compared to alumina particles, which resulted in a nearly 10-fold increase in the surface normalized adsorption of arsenate ($AsO_4^{3-}$) on nanoporous alumina (Wang, 2014). The modification of surface charge of aluminol in nanopores can also cause an increase in the adsorption of iodate on halloysite.

Worldwide, Large halloysite deposits have been found in China, the United States, Australia, New Zealand, Brazil and Mexico (Joussein et al., 2005). With the excellent $IO_3^-$ adsorption performance and low cost, halloysite has the potential to be an adsorbent on the adsorption of radioactive iodate in natural and engineered environments. This work and several previous works (Jung et al., 2012, 2016, 2019; Knight et al., 2018) have demonstrated that nanopores can significantly modify mineral-water interface chemistry. As nanopores are ubiquitous in natural environmental media including minerals, rocks, soils, and sediments (Wang, 2014; Deng et al., 2017), they may play an important role in retarding $IO_3^-$ movement in environment. For prediction of the migration and fate of iodine geochemistry as well as risk or performance assessment of radioactive iodine, it may be important to keep in mind that the nanopores are very important besides chemical compositions of minerals.

## 4. Conclusions

In this study, the adsorption of $IO_3^-$ on halloysite was investigated for the first time. The nanosized tubular halloysite exhibited higher adsorption capacity and stronger adsorption to $IO_3^-$ than the platy kaolinite. The specific surface area normalized $K_d$ values of halloysite are 13.5 times higher than that of kaolinite. < 23% of pre-adsorbed $IO_3^-$ was released from halloysite after 48 h desorption. In contrast, > 90% of pre-adsorbed $IO_3^-$ was removed from kaolinite after 1 h desorption. What is more, halloysite had high selectivity to $IO_3^-$, and the adsorption capacity on halloysite is slightly affected by the concurrent anions. These results are attributed to the curved octahedral sheet in the inner surface of halloysite nanotubes. It is proposed that the curved octahedral sheet caused geometry match between three oxygen atoms in the iodate and three OH above the vacant site of the octahedral sheet. With the excellent $IO_3^-$ adsorption performance and low cost, halloysite is a potential adsorbent for immobilizing radioactive iodate in natural and engineered environments. Future works should address molecular-scale speciation of $IO_3^-$ associated with halloysite lumen surface, using spectroscopic approaches.

## Declaration of Competing Interest

The authors declare no competing financial interest.

## Acknowledgments

This work was supported by the National Natural Science Foundation of China (Grant No. 41603065 and 41473064), CAS “Light of West China” Program, Guizhou Provincial Science and Technology Project (No. [2019]1318), and Department of Geoscience at the University of Wisconsin–Madison.

## Authors' contributions

Huifang Xu conceived concept, co-designed experiments, and analyzed data.

Wenbi Yu designed experiments, carried out adsorption and desorption experiments, analyzed data, and drafted manuscript.

Daoyong Tan carried out TEM results of halloysite samples.

Yihang Fang carried out TEM results of kaolinite and helped XRD experiments.

Eric E. Roden co-designed sorprion experiments.

Quan Wan analyzed pore sizes of the samples.

All the authors contributed to manuscript writing.

## References

Anastopoulos, I., Mittal, A., Usman, M., Mittal, J., Yu, G., Núñez-Delgado, A., Kornaros, M., 2018. A review on halloysite-based adsorbents to remove pollutants in water and wastewater. J. Mol. Liq. 269, 855–868.
Hydrous phyllosilicates (exclusive of micas). In: Bailey, S. (Ed.), Reviews in Mineralogy. vol. 19. Mineralogical Society of America, Washington, DC, pp. 725.
Barrett, E.P., Joyner, L.G., Halenda, P.P., 1951. The determination of pore volume and area distributions in porous substances. I. Computations from nitrogen isotherms. J. Am. Chem. Soc. 73, 373–380.
Bates, T.F., Hildebrand, F.A., Swineford, A., 1950. Morphology and structure of endellite and halloysite. Am. Mineral. 35, 463–484.
Bish, D.L., 1993. Rietveld refinement of the kaolinite structure at 1.5 K. Clay Clay Miner. 41, 738–744.
Brunauer, S., Emmett, P.H., Teller, E., 1938. Adsorption of gases in multimolecular layers. J. Am. Chem. Soc. 60, 309–319.
Bujňáková, Z., Baláž, P., Zorkovská, A., Sayagués, M.J., Kováč, J., Timko, M., 2013. Arsenic sorption by nanocrystalline magnetite: an example of environmentally promising interface with geosphere. J.Hazard. Mater. 262, 1204–1212.
Castellano, M., Turturro, A., Riani, P., Montanari, T., Finocchio, E., Ramis, G., Busca, G., 2010. Bulk and surface properties of commercial kaolins. Appl. Clay Sci. 48, 446–454.
Choung, S., Um, W., Kim, M., Kim, M.G., 2013. Uptake Mechanism for Iodine Species to Black Carbon. Environ. Sci. Technol. 47, 10349–10355.
Couture, R.A., Seitz, M.G., 1983. Sorption of anions of iodine by iron oxides and kaolinite. Nucl. Chem. Waste Manage. 4, 301–306.
Dai, J.-L., Zhang, M., Zhu, Y.-G., 2004. Adsorption and desorption of iodine by various Chinese soils. I. Iodate. Environ. Int. 30, 525–530.
Dai, J.L., Zhang, M., Hu, Q.H., Huang, Y.Z., Wang, R.Q., Zhu, Y.G., 2009. Adsorption and desorption of iodine by various Chinese soils: II. Iodide and iodate. Geoderma 153, 130–135.
Deng, L.L., Yuan, P., Liu, D., Annabi-Bergaya, F., Zhou, J.M., Chen, F.R., Liu, Z.W., 2017. Effects of microstructure of clay minerals, montmorillonite, kaolinite and halloysite, on their benzene adsorption behaviors. Appl. Clay Sci. 143, 184–191.
Deng, L.L., Yuan, P., Liu, D., Du, P., Zhou, J., Wei, Y., Song, Y., Liu, Y., 2019. Effects of calcination and acid treatment on improving benzene adsorption performance of halloysite. Appl. Clay Sci. 181, 105240.
Drever, J.I., Marion, G., 1998. The geochemistry of natural waters: surface and groundwater environments. J. Environ.Qual. 27, 245.
Fuge, R., 2013. Soils and Iodine Deficiency. In: Selinus, O. (Ed.), Essentials of Medical Geology, Revised edition. Springer Netherlands, Dordrecht, pp. 417–432.
Fuge, R., Johnson, C.C., 2015. Iodine and human health, the role of environmental geochemistry and diet, a review. Appl. Geochem. 63, 282–302.
Ghose, S., Wan, C., 1978. Salesite, $CuIO_3(OH)$, and Cu $(IO_3)_2{\cdot}2H_2O$; a comparison of the crystal structures and their magnetic behavior. Am. Mineral. 63, 172–179.
Goldberg, S., Davis, J.A., Hem, J.D., 1996. The surface chemistry of aluminum oxides and hydroxides. Environ. Chem. Aluminum 271–331.
Gregg, S., Sing, K., SW, A., 1982. Surface Area and Porosity. Academic Press Inc. Ltd, London, pp. 111–194.
Hao, W., Flynn, S.L., Alessi, D.S., Konhauser, K.O., 2018. Change of the point of zero net proton charge ($pH_{PZNPC}$) of clay minerals with ionic strength. Chem. Geol. 493, 458–467.
Iglesias, L., Álvarez, M.G., Chimentão, R.J., Leganés, J.L., Medina, F., 2014. On the role of ultrasound and mechanical stirring for iodide adsorption by calcined layered double hydroxides. Appl. Clay Sci. 91-92, 70–78.
Joussein, E., Petit, S., Churchman, J., Theng, B., Righi, D., Delvaux, B., 2005. Halloysite clay minerals–a review. Clay Miner. 40, 383–426.
Jung, H.B., Boyanov, M.I., Konishi, H., Sun, Y.B., Mishra, B., Kemner, K.M., Roden, E.E., Xu, H.F., 2012. Redox Behavior of Uranium at the Nanoporous Aluminum Oxide-Water Interface: Implications for Uranium Remediation. Environ. Sci. Technol. 46, 7301–7309.
Jung, H.B., Xu, H., Konishi, Roden, E, E., 2016. Role of nano-goethite in controlling U(VI) sorptin-desorption in subsurafce soil. J.Geochem. Explor. 169, 80–88.
Jung, H.B., Xu, H., Roden, E.E., 2019. Long-term sorption and desorption of uranium in sapolite subsoil with nanoporous goethite. Appl. Geochem. 102, 129–138.
Kaplan, D.I., 2003. Influence of surface charge of an Fe-oxide and an organic matter dominated soil on iodide and pertechnetate sorption. Radiochim. Acta 91, 173–178.
Kaplan, D.I., Serne, R.J., Parker, K.E., Kutnyakov, I.V., 2000. Iodide Sorption to Subsurface Sediments and Illitic Minerals. Environ. Sci. Technol. 34, 399–405.
Kaplan, D.I., Denham, M.E., Zhang, S., Yeager, C., Xu, C., Schwehr, K., Li, H.-P., Ho, Y.-F., Wellman, D., Santschi, P.H., 2014. Radioiodine biogeochemistry and prevalence in groundwater. Crit. Rev. Environ. Sci. Technol. 44, 2287–2335.
Knight, A.W., Tigges, A.B., Ilgen, A.G., 2018. Adsorption of copper (II) on mesoporous silica: the effect of nano-scale confinement. Geochem. Trans. 19, 13.
Kohyama, N., Fukushima, K., Fukami, A., 1978. Observation of the Hydrated form of tubular halloysite by an electron microscope equipped with an environmental cell. Clay Clay Miner. 26, 25–40.
Levinger, N.E., 2002. Water in confinement. Science 298, 1722–1723.
Li, D., Kaplan, D.I., Sams, A., Powell, B.A., Knox, A.S., 2018. Removal capacity and chemical speciation of groundwater iodide ($I^-$) and iodate ($IO_3^-$) sequestered by

organoclays and granular activated carbon. J. Environ. Radioact. 192, 505–512.
Liang, X., Wei, G., Xiong, J., Tan, F., He, H., Qu, C., Yin, H., Zhu, J., Zhu, R., Qin, Z., Zhang, J., 2017. Adsorption isotherm, mechanism, and geometry of Pb(II) on magnetites substituted with transition metals. Chem. Geol. 470, 132–140.
Limousin, G., Gaudet, J.-P., Charlet, L., Szenknect, S., Barthes, V., Krimissa, M., 2007. Sorption isotherms: a review on physical bases, modeling and measurement. Appl. Geochem. 22, 249–275.
Liu, D., Yuan, P., Tan, D.Y., Liu, H.M., Wang, T., Fan, M.D., Zhu, J.X., He, H.P., 2012. Facile preparation of hierarchically porous carbon using diatomite as both template and catalyst and methylene blue adsorption of carbon products. J. Colloid Interface Sci. 388, 176–184.
Liu, Y., Gu, P., Jia, L., Zhang, G., 2016. An investigation into the use of cuprous chloride for the removal of radioactive iodide from aqueous solutions. J. Hazard. Mater. 302, 82–89.
Longombe, A.O., Geelhoed, G.W., 1997. Iodine deficiency disorders and infertility in Northeast Zaire. Nutrition 4, 342–343.
Mahmudov, R., Huang, C.P., 2011. Selective adsorption of oxyanions on activated carbon exemplified by Filtrasorb 400 (F400). Sep. Purif. Technol. 77, 294–300.
Matusik, J., 2014. Arsenate, orthophosphate, sulfate, and nitrate sorption equilibria and kinetics for halloysite and kaolinites with an induced positive charge. Chem. Eng. J. 246, 244–253.
Matusik, J., 2016. Chapter 23 - Halloysite for Adsorption and Pollution Remediation. In: Yuan, P., Thill, A., Bergaya, F. (Eds.), Developments in Clay Science. Elsevier, pp. 606–627.
Miller, A., Kruichak, J., Mills, M., Wang, Y., 2015. Iodide uptake by negatively charged clay interlayers? J. Environ. Radioact. 147, 108–114.
Nagata, T., Fukushi, K., 2010. Prediction of iodate adsorption and surface speciation on oxides by surface complexation modeling. Geochim. Cosmochim. Acta 74, 6000–6013.
Nie, G., Pan, B., Zhang, S., Pan, B., 2013. Surface Chemistry of Nanosized Hydrated Ferric Oxide Encapsulated inside Porous Polymer: Modeling and Experimental Studies. J. Phys. Chem. C 117, 6201–6209.
Pasbakhsh, P., Churchman, G.J., Keeling, J.L., 2013. Characterisation of properties of various halloysites relevant to their use as nanotubes and microfibre fillers. Appl. Clay Sci. 74, 47–57.
Rao, S.M., Sridharan, A., 1984. Mechanism of sulfate adsorption by kaolinite. Clay Clay Miner. 32, 414–418.
Riebe, B., Dultz, S., Bunnenberg, C., 2005. Temperature effects on iodine adsorption on organo-clay minerals: I. Influence of pretreatment and adsorption temperature. Appl. Clay Sci. 28, 9–16.
Riese, A.C., 1982. Adsorption of radium and thorium onto quartz and kaolinite. a comparison of solution/surface equilibria models. In: Colorado School of Mines. Arthur Lakes Library.
Schroth, B.K., Sposito, G., 1997. Surface Charge Properties of Kaolinite. Clay Clay Miner. 45, 85–91.
Sposito, G., 1984. The Surface Chemistry of Soils. Oxford university press.
Stumm, W., 1992. Chemistry of the Solid-Water Interface. Wiley, New York.
Tan, D., Yuan, P., Annabi-Bergaya, F., Dong, F., Liu, D., He, H., 2015. A comparative study of tubular halloysite and platy kaolinite as carriers for the loading and release of the herbicide amitrole. Appl. Clay Sci. 114, 190–196.
Tarı, G., Bobos, I., Gomes, C.S., Ferreira, J.M., 1999. Modification of surface charge properties during kaolinite to halloysite-7Å transformation. J. Colloid Interface Sci. 210, 360–366.
Ticknor, K., Cho, Y.-H., 1990. Interaction of iodide and iodate with granitic fracture-filling minerals. J. Radioanal. Nucl. Chem. 140, 75–90.
Von Hippel, F.N., 2011. The radiological and psychological consequences of the Fukushima Daiichi accident. Bull. At. Sci. 67, 27–36.
Wang, Y., 2014. Nanogeochemistry: Nanostructures, emergent properties and their control on geochemical reactions and mass transfers. Chem. Geol. 378–379, 1–23.
Wang, Y., Bryan, C., Xu, H., Pohl, P., Yang, Y., Brinker, C.J., 2002. Interface chemistry of nanostructured materials: Ion adsorption on mesoporous alumina. J. Colloid Interface Sci. 254, 23–30.
Weber, T.W., Chakravorti, R.K., 1974. Pore and solid diffusion models for fixed-bed adsorbers. AICHE J. 20, 228–238.
Wei, Y.F., Yuan, P., Liu, D., Losic, D.S., Tan, D.Y., Chen, F.R., Liu, H.C., Zhou, J.M., Du, P.X., Song, Y.R., 2019. Activation of natural halloysite nanotubes by introducing lanthanum oxycarbonate nanoparticles via co-calcination for outstanding phosphate removal. Chem. Commun. 55, 2110–2113.
Westall, J., Hohl, H., 1980. A comparison of electrostatic models for the oxide/solution interface. Adv. Colloid Interf. Sci. 12, 265–294.
Xi, Y., Mallavarapu, M., Naidu, R., 2010. Preparation, characterization of surfactants modified clay minerals and nitrate adsorption. Appl. Clay Sci. 48, 92–96.
Xu, H., Xu, D.C., Wang, Y., 2017. Natural Indices for the Chemical Hardness/Softness of Metal Cations and Ligands. ACS Omega 2, 7185–7193.
Yu, W., Xu, H., Roden, E.E., Wan, Q., 2019. Efficient adsorption of iodide from water by chrysotile bundles with wedge-shaped nanopores. Appl. Clay Sci. 183, 105331.
Yuan, P., Southon, P.D., Liu, Z., Green, M.E., Hook, J.M., Antill, S.J., Kepert, C.J., 2008. Functionalization of halloysite clay nanotubes by grafting with γ-aminopropyltriethoxysilane. J. Phys. Chem. C 112, 15742–15751.
Yuan, P., Liu, D., Tan, D.-Y., Liu, K.-K., Yu, H.-G., Zhong, Y.-H., Yuan, A.-H., Yu, W.-B., He, H.-P., 2013. Surface silylation of mesoporous/macroporous diatomite (diatomaceous earth) and its function in Cu (II) adsorption: the effects of heating pretreatment. Microporous Mesoporous Mater. 170, 9–19.
Yuan, P., Tan, D., Annabi-Bergaya, F., 2015. Properties and applications of halloysite nanotubes: recent research advances and future prospects. Appl. Clay Sci. 112-113, 75–93.
Zhang, Y., Fu, L., Yang, H., 2012. Insights into the physicochemical aspects from natural halloysite to silica nanotubes. Colloids Surf. A Physicochem. Eng. Asp. 414, 115–119.
Zhang, S., Xu, C., Creeley, D., Ho, Y.-F., Li, H.-P., Grandbois, R., Schwehr, K.A., Kaplan, D.I., Yeager, C.M., Wellman, D., Santschi, P.H., 2013. Iodine-129 and Iodine-127 Speciation in Groundwater at the Hanford Site, U.S.: Iodate Incorporation into Calcite. Environ. Sci. Technol. 47, 9635–9642.